A phase retrieval framework to directly reconstruct the projected refractive index

Felix Wittwer[1,2,5,*], Johannes Hagemann[1,3], Dennis Brückner[1,2,3], Silja Flenner[4], and Christian G. Schroer[1,2,3]

[1]*Center for X-ray and Nano Science (CXNS), Deutsches Elektronen-Synchrotron DESY, Notkestraße 85, 22607 Hamburg, Germany*
[2]*Department Physik, Universität Hamburg, Luruper Chaussee 149, 22761 Hamburg, Germany*
[3]*Helmholtz Imaging Platform, Deutsches Elektronen-Synchrotron DESY, Notkestraße 85, 22607 Hamburg, Germany*
[4]*Helmholtz-Zentrum Hereon, Max-Planck-Str. 1, 21502 Geesthacht, Germany*
[5]*Current address: NERSC, Lawrence Berkeley National Laboratory, Berkeley, California 94720, USA*
[*]*Corresponding author: wittwer@xray-lens.de*

Abstract: We present in this article a phase retrieval framework to recover amplitude and phase of an object's transmission rather than the complex wave-field behind the object. This avoids the common phase unwrapping problem. It is straightforward to integrate the refractive framework into conventional iterative phase retrieval algorithms. As examples, we introduce refractive algorithms for ptychography, holography and coherent diffraction imaging. The method is demonstrated using measured data from ptychography and near-field holography.

1. Introduction

Phase retrieval (PR), i.e., the recovery of a complex-valued signal from intensity-only measurements, is an ubiquitous task in physics and engineering [1–5]. It is used wherever detectors are not fast enough to measure the oscillations of a signal of interest. PR is therefore especially prevalent in electron [6] and X-ray microscopy [7–10], but it also finds applications in terahertz imaging [11] and optical microscopy [12]. Today, a wide range of phase retrieval techniques have been developed to image samples in different experimental situations [13–15].

Commonly, the object of interest is nearly transparent and shows little absorption contrast. This is a frequent problem in hard X-ray microscopy, especially for biological specimens [16]. Nevertheless, the object imprints a phase shift on the transmitted wave. At multi-keV photon energies, this signal can be orders of magnitude higher than the absorption. For this reason, the phase shift is often more important than the absorption to produce an image of the sample, if it can be recovered from the measurements. Notably, PR recovers not only the absorption but also the phase shift, which makes PR ideally suited to image otherwise invisible objects. While phase contrast techniques such as speckle tracking [17] or edge enhancement [18] allow one to directly measure the refractive index of the sample, they lack the increase in resolution that PR techniques such as holography [19] or ptychography [20] offer.

In conventional phase retrieval, the complex wave field behind the object is typically reconstructed. When considering this complex wave field, the phase shift cannot be uniquely recovered, as adding or subtracting multiples of 2π is indistinguishable from the ground truth. The reconstructed phase is therefore wrapped to a range of 2π for thick samples with a large phase shift. The phase wrapping poses a challenge, especially for computed tomography, as each projection must be unwrapped prior to tomographic reconstruction [21]. The success of phase unwrapping is highly dependent on the quality of the phase reconstruction, in particular in the presence of phase vortices [22, 23].

An alternative way that avoids the problematic phase unwrapping altogether has been proposed

by Chowdhury *et al.* for Fourier ptychography [24]. In general, PR methods reconstruct the complex transmission of the sample. Instead of the transmission, the proposed refractive framework directly reconstructs the projected refractive index of the sample. The projection is the logarithm of the transmission, scaled by $k = 2\pi/\lambda$. Particularly, the projected refractive index is no longer bound to a range of 2π and is linearly related to the refractive index. This last property is beneficial for complex PR schemes that couple multiple scans into one reconstruction [25–27].

In this work, we generalize the idea of refractive phase retrieval and apply it to three popular PR techniques: ptychography [20, 28], near-field holography (NFH) [19, 29] and coherent diffraction imaging (CDI) [30]. Additionally, we provide a series of steps how refractive variants for other phase retrieval algorithms can be constructed. We demonstrate the performance of refractive ptychography, refractive holography and refractive CDI on simulated and experimental data from X-ray microscopy experiments at the beamlines P05 and P06 of the synchrotron radiation source PETRA III in Hamburg, Germany. While these demonstrations all use hard X-rays, all arguments are transferable to other photon energies and to electrons.

2. Refractive Framework

X-rays interact only weakly with matter due to their high energy. Owing to this weak interaction, the refractive index for X-rays differs only marginally from unity. Because only this difference is important, the refractive index is commonly written as

$$n = 1 - \delta + \mathrm{i}\beta. \tag{1}$$

Both the refractive index decrement δ and the absorption index β are on the order of 10^{-5} to 10^{-6} and smaller. For a thin sample, the imaging contrast at a point $\mathbf{r} = (x, y)$ is given by the transmission or object function

$$O_{\mathbf{r}} = A_{\mathbf{r}} \cdot \exp(\mathrm{i}\Phi_{\mathbf{r}}) = \exp\left(\mathrm{i}k \int n - 1 \,\mathrm{d}z\right), \tag{2}$$

which projects the refractive index along the optical axis z. The goal of conventional PR is to recover $O_{\mathbf{r}}$. For refractive PR, the aim is to reconstruct the refractive object function

$$\widetilde{O}_{\mathbf{r}} = k \int n - 1 \,\mathrm{d}z = -k \int \delta \,\mathrm{d}z + \mathrm{i}k \int \beta \,\mathrm{d}z. \tag{3}$$

This function is related to the conventional $O_{\mathbf{r}}$ through a complex exponential

$$O_{\mathbf{r}} = \exp\left(\mathrm{i}\widetilde{O}_{\mathbf{r}}\right). \tag{4}$$

Due to this relationship, the phase shift $\Phi_{\mathbf{r}}$ and the amplitude $A_{\mathbf{r}}$ are respectively associated with the real and imaginary component of the refractive object

$$\Phi_{\mathbf{r}} = \Re(\widetilde{O}_{\mathbf{r}}) = -k \int \delta \,\mathrm{d}z, \tag{5}$$

$$-\ln(A_{\mathbf{r}}) = \Im(\widetilde{O}_{\mathbf{r}}) = k \int \beta \,\mathrm{d}z. \tag{6}$$

Unlike Φ, the real part of the refractive object has the advantage that it is not limited to a specific range. It can therefore recover the sample without phase wraps. This makes refractive PR well suited to reconstruct large samples.

2.1. Refractive Phase Retrieval

The successful reconstruction of the object function is contingent on solving the phase problem. Because no closed-form solution exists, many PR algorithms follow an error reduction strategy. This iterative strategy approximates the object function to simulate the diffraction process. In each iteration, the approximate object function is improved so that the error

$$L = \sum_j d(I_j, M_j) \tag{7}$$

is reduced, according to a metric d between the modeled images I_j and the measured diffraction images M_j.

The improvement is determined by the gradient of the error function. For the refractive framework, we use Wirtinger derivatives [31] to calculate the gradient with respect to the refractive object:

$$\frac{\partial L}{\partial \widetilde{O}_\mathbf{r}} = \frac{\partial L}{\partial O_\mathbf{r}} \cdot \frac{\partial O_\mathbf{r}}{\partial \widetilde{O}_\mathbf{r}} = \frac{\partial L}{\partial O_\mathbf{r}} \cdot \mathrm{i}O_\mathbf{r}. \tag{8}$$

Notably, the refractive gradient is nearly identical to the conventional gradient, except for a simple multiplication with the object function O and the imaginary unit. As a result, many conventional PR algorithms can be readily converted to the refractive framework by simply multiplying the object modification with $\mathrm{i}O$. We demonstrate this in the following sections by presenting refractive algorithms for ptychography, holography, and CDI.

3. Refractive Ptychography

Ptychography combines scanning microscopy with coherent diffraction imaging to solve the phase problem [13, 20]. A typical ptychographic scanning setup is shown in Fig. 1(a). To reconstruct the refractive object from the diffraction patterns, we introduce here the refractive ptychographic iterative engine (refPIE), an advancement of the widely used extended ptychographic iterative engine (ePIE) [32]. A detailed derivation of refPIE is given in [33]. Refractive extensions to other algorithms like 3PIE [34], multi-modal ptychography [35], etc. can be straightforwardly obtained, using refPIE as a template.

Similar to ePIE and other ptychography algorithms [20], refPIE starts from initial guesses $\widetilde{O}_0$ and P_0 for the refractive object and probe function. In the reconstruction, the update steps are repeated until $\widetilde{O}$ and P converge:

1. Randomly choose a diffraction pattern M_j that was not yet processed.
2. Using the corresponding scan point $\mathbf{R}_j$, calculate the exit wave:

$$\psi_\mathbf{r} = \exp\left(\mathrm{i}\widetilde{O}_\mathbf{r}\right) \cdot P_{\mathbf{r}-\mathbf{R}_j} \tag{9}$$

3. Propagate the scattered wave to the detector, using the Fourier transform (far field) or Fresnel propagation (near field):

$$\Psi_\mathbf{q} = \mathcal{F}\left(\psi_\mathbf{r}\right) \tag{10}$$

4. Replace the simulated amplitude with the measured diffraction pattern, only keeping the phase of Ψ:

$$\Psi'_\mathbf{q} = \sqrt{M_{j,\mathbf{q}}} \cdot \frac{\Psi_\mathbf{q}}{\left|\Psi_\mathbf{q}\right|} \tag{11}$$

5. Propagate the updated wave back to the sample plane:

$$\psi'_\mathbf{r} = \mathcal{F}^{-1}\left(\Psi'_\mathbf{q}\right) \tag{12}$$

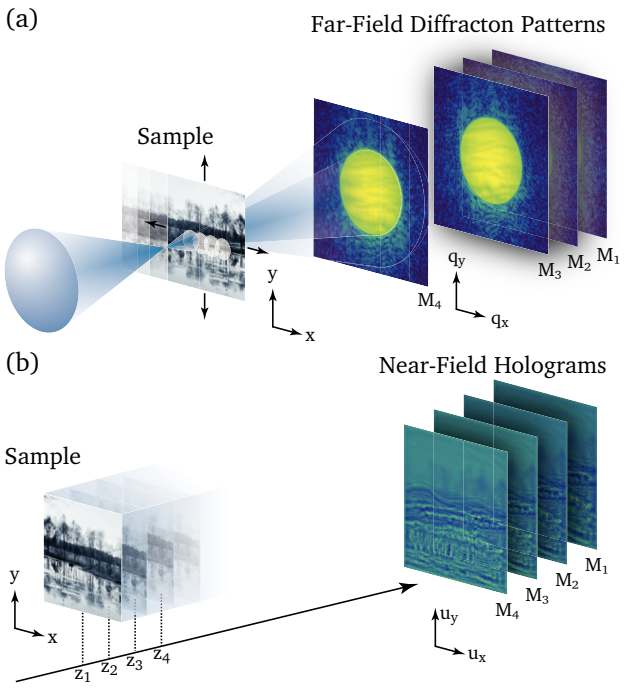

Fig. 1. Experimental setups for (a) ptychography and (b) inline holography. (a) In ptychography, the sample is scanned transversal to the beam direction. For each scan point $\mathbf{R}_j$, the detector records the far-field diffraction pattern M_j. For a successful reconstruction, the beam footprints from adjacent scan points should overlap. This ensures that the corresponding diffraction patterns share information. (b) In holography, the sample is moved along the beam direction to different defocus distances z_j, each giving rise to a different hologram M_j due to the change in the Fresnel number Fr_j.

6. At the end, update the refractive object and the probe with the updated exit wave (the parameters α and β tune the update strength):

$$\widetilde{O}_{\mathbf{r}} \leftarrow \widetilde{O}_{\mathbf{r}} + \alpha \frac{\left(\mathrm{i}\psi_{\mathbf{r}-\mathbf{R}_j}\right)^*}{\max\left|\psi_{\mathbf{r}-\mathbf{R}_j}\right|^2} \cdot \left(\psi'_{\mathbf{r}} - \psi_{\mathbf{r}}\right) \tag{13a}$$

$$P_{\mathbf{r}} \leftarrow P_{\mathbf{r}} + \beta \frac{\exp\left(-\mathrm{i}\widetilde{O}^*_{\mathbf{r}+\mathbf{R}_j}\right)}{\max\left|\exp\left(\mathrm{i}\widetilde{O}_{\mathbf{r}+\mathbf{R}_j}\right)\right|^2} \cdot \left(\psi'_{\mathbf{r}} - \psi_{\mathbf{r}}\right) \tag{13b}$$

One iteration is complete when there are no more patterns to process. Before the next iteration starts, all patterns are again marked as unprocessed. Typically, the reconstruction converges after one hundred up to one thousand iterations.

Most steps of refPIE are identical to other ptychography algorithms. The unique difference and central feature of refPIE is Eq. (13a), where the difference $\psi' - \psi$ is conventionally multiplied with the complex conjugated probe P. Here, P is replaced with $\mathrm{i}\psi$, the exit wave multiplied with the imaginary unit. The proof that this exchange leads to a refractive reconstruction follows from Eq. (8) as $P \cdot \mathrm{i}O = \mathrm{i}\psi$. The complex conjugation is due to the nature of Wirtinger derivatives.

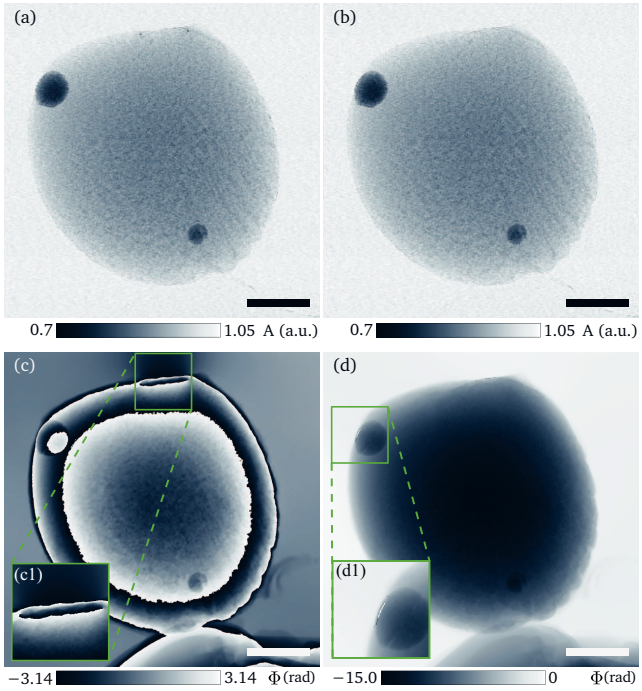

Fig. 2. Ptychographic reconstruction of the micrometeorite. (a) and (b) modulus of the micrometeorite obtained by ePIE and refPIE, respectively. (c) and (c1) phase of the ePIE reconstruction. The reconstruction shows strong phase wrapping and the detail (c1) shows a pair of phase vortices. (d) and (d1) phase of the refPIE reconstruction. The phases are in the correct range without any unwrapping applied. The detail (d1) shows an artifact in the top left of the refPIE reconstruction. This artifact is offset by $\pm 2\pi$ to the rest of the meteorite and can easily be fixed. The scale bars represent 20 µm.

3.1. Micrometeorite Experiment

We demonstrate the capabilities of refPIE on a ptychography scan of a micrometeorite. The experiment was carried out at beamline P06 of PETRA III (DESY, Hamburg), using the combined Micro-Nanoprobe setup to maximize the detector distance [36]. The 18 keV X-ray beam was focused by a pair of Kirkpatrick-Baez mirrors, focal length 250 mm, to a full-width at half maximum spot size of 110 nm × 110 nm, as obtained from the ptychographic reconstruction. The sample was placed 500 µm behind the focus where the beam had expanded so that 50 % of the total beam intensity fell within a 190 nm × 190 nm circle. The micrometeorite has a diameter of about 80 µm. To quickly scan a sample of this size, the scanning stage never stopped and moved the micrometeorite in a continuous zigzag path across the beam. These fly-scans allow acquisition rates in the kilohertz range [37–40]. The micrometeorite was scanned over a 100 µm × 100 µm area with 1 ms exposure for each diffraction pattern. The velocity of the stage was set to 200 µm s^{-1} so that the micrometeorite moved 200 nm during one exposure. Each new line was vertically offset by the same amount of 200 nm. The scan recorded more than a quarter of a million diffraction patterns in under 9.5 min. The diffraction patterns were recorded with an Eiger 500k situated 8.75 m downstream of the sample in the Nanoprobe hutch. A 7 m long evacuated flight tube between sample and detector reduced air scattering on the detector. The reconstructions use the central 128 × 128 pixels of the Eiger images, resulting in a pixel size of 62.8 nm in the ptychographic reconstruction. All experimental parameters are summarized in

Table 1.

Table 1. Parameters of the micrometeorite experiment.

Parameters	**Value**
Energy	18 keV
Flux	3.75×10^8/s
Exposure	1 ms
Scan size	100 µm × 100 µm
Step size	200 nm × 200 nm
Probe diameter	190 nm
Detector distance	8752 mm
Detector pixel	75 µm × 75 µm
Image size	128 × 128 pixels
Pixel size (rec.)	62.8 nm

We reconstruct the scan twice: once with the conventional ePIE algorithm, once with refPIE. Since the probe is very small compared to the scan size, both algorithms converge slowly. To improve the reconstruction speed, we similarly modified both algorithms. First, we adapted the parallel ptychography variant described in [41, 42] for ePIE and refPIE. We also constrained the object modulus to only range from 0.2 to 2.0. And lastly we used momentum accelerated gradients for both algorithms, as described in [43–45]. We set the momentum damping factors η_{obj} and η_{prb} to 0.98 and applied the momentum in every second iteration.

Both algorithms run for 1000 iterations, the reconstructed sample amplitudes and phase shifts are shown in Fig. 2. The ePIE reconstruction shows phase wraps and two phase vortices at the top of the meteorite, shown in the inset. These singularities are especially problematic for tomographic reconstructions. In contrast, the discontinuities and phase wrap problems are solved in the refPIE reconstruction. The real part, shown in Fig. 2(d), is continuous and shows no phase wrapping, despite a maximum phase shift of close to 15 rad. Two small areas at the top and the left contain offset values, see Fig. 2(d1). These areas have the largest phase gradients and both ePIE and refPIE struggle in the reconstruction. The left area is simply offset by 2π, which can be easily fixed. The top area corresponds to the vortices in the ePIE reconstruction and demonstrates that refPIE is able to isolate problematic regions and reconstruct the unaffected parts of the sample without detriments.

4. Refractive Near-Field Holography

Near-field holography (NFH) is a full-field imaging scheme which can be implemented in a parallel beam setting or, to achieve higher magnifications, in the divergent beam of nano-focusing optics. A principal sketch of a holography setup is shown in Fig. 1(b). NFH allows for single-exposure acquisitions of extended objects and is thus a promising method to image ultra-short processes [46, 47] and radiation-sensitive samples [48]. Weak samples, i.e., thin objects with negligible absorption and a total phase shift smaller than π, can be reconstructed from a single hologram. To reconstruct strongly scattering samples, multiple holograms M_j at different Fresnel numbers Fr_j are necessary.

We use an alternating projection (AP) algorithm given by

$$\widetilde{O}_{i+1} = \tilde{P}_S(\tilde{P}_M(\widetilde{O}_i)), \tag{14}$$

where the sample constraint $\tilde{P}_S$ constricts the reconstruction in the sample plane and the magnitude projector $\tilde{P}_M$ ensures that the reconstruction fits to the measurement and is defined as

$$\tilde{P}_M(\widetilde{O}_i) := \widetilde{O}_i - \Delta\widetilde{O}. \tag{15}$$

Common sample constraint choices are the support, i.e. the outline of the sample, or a vanishing absorption, i.e. a pure-phase sample. These constraints can be readily adapted for the refractive framework. Notably, the homogeneity constraint or single material constraint [18, 49] can be directly expressed in the refractive framework as a constant ratio between δ and β or $\Re(\widetilde{O})$ and $\Im(\widetilde{O})$, respectively. Concerning Eq. (15), the main difference to conventional holography algorithms is the object update

$$\Delta\widetilde{O} := -\frac{\mathrm{i}O_i^*}{J \max|O_i|^2} \sum_{j=1}^{J} \mathcal{D}_{\mathrm{Fr}_j}^{-1}\left(\mathcal{D}_{\mathrm{Fr}_j}(O_i) \cdot \left[1 - \sqrt{M_j/I_j}\right]\right), \tag{16}$$

where * denotes the complex conjugate, $\mathcal{D}_{\mathrm{Fr}}$ is the Fresnel propagator, M_j denotes the measured hologram and $I_j = |\mathcal{D}_{\mathrm{Fr}}(O)|^2$ the current estimate for M_j and J the number of measurements. For a detailed derivation we refer to [33]. Equation (16) averages the refractive update from all holograms, yielding an improved resistance against noise. Alternatively, the object can be updated in a sequential manner for each hologram individually. For the experimental demonstration, we implemented the parallel variant in the Holotomo Toolbox [50, 51].

As in ptychography, reconstructing the low-spatial frequencies requires the most iterations in holography. To accelerate this, we combine Eq. (14) with a Nesterov gradient step [43, 44].

4.1. Ivory Experiment

Table 2. Parameters of the ivory experiment.

Parameter	**Value**
Energy	11 keV
Exposure/hologram	1 s
Field of view	112 µm × 70 µm
Defocus distance	138.6 mm and 139.6 mm
Detector distance	16.33 m
Magnification	118
Detector pixel size	6.5 µm × 6.5 µm
Effective pixel size	55 nm × 55 nm
Image size	2048 × 2048 pixels

We demonstrate the capabilities of refractive holography using an ivory sample. The NFH data were obtained at the nano branch of beamline P05 operated by the Helmholtz-Zentrum Hereon located at PETRA III at DESY, Hamburg. The measurement was carried out at a photon energy

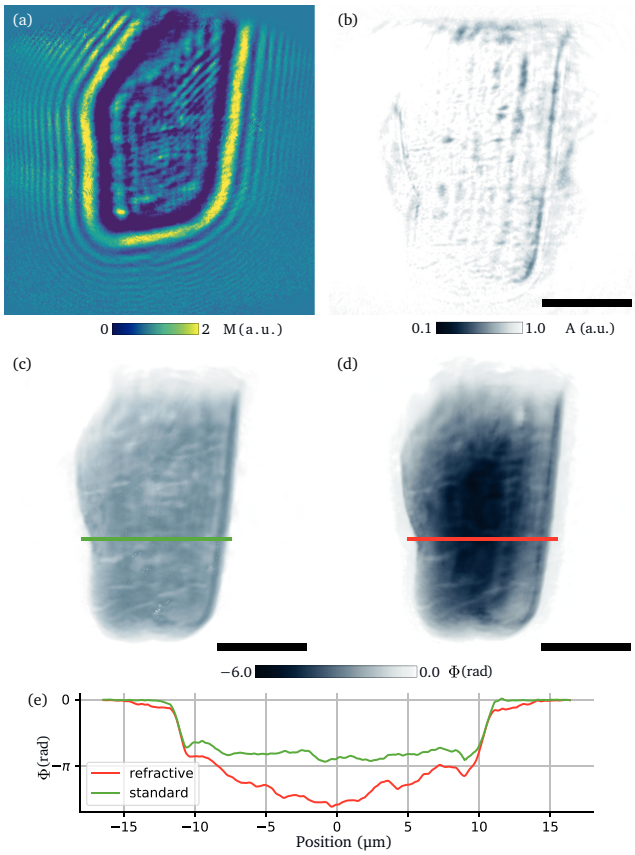

Fig. 3. Results for NFH from experimental data of an ivory sample. (a) flat-field corrected hologram of the ivory for the 138.6 mm defocus distance. (b) the amplitudes obtained by calculating the exponential of $\Im(\widetilde{O})$. Surface regions with gallium depositions show significant absorption. (c) phase of the conventional reconstruction, not extending to the full phase range. (d) phase of the refractive reconstruction, spanning a range of nearly 2π. The colorbar below (c) and (d) applies to both panels. (e) comparison of two phase profiles from (c) and (d), the green and red lines indicate the location of the profiles. All scalebars represent 10 μm.

of $E = 11$ keV. The detector was a Hamamatsu C12849-101U with a 10 µm Gadox scintillator and a pixel size of 6.5 µm. It was placed 16.33 m behind the focus of a Fresnel zone plate with a diameter of 300 µm and an outermost zone width of 50 nm [52]. The sample was placed 138.6 mm and 139.6 mm behind the focus to gather diverse data for the reconstruction. This yields a 118× magnification with an effective pixel size of 55 nm. All parameters are summarized in Table 2.

For comparison we reconstructed the ivory with a conventional algorithm and with the refractive framework. Before the reconstruction, the holograms were flat-field corrected, see Fig. 3(a), rescaled to the same pixel-size using the Fresnel scaling theorem, and aligned. The constraints in the sample plane $\tilde{P}_S$ were a combination of value clamping and support. The allowed ranges were $\Phi \in [-10, 0.01]$ rad and $\Im(\widetilde{O}) \in [-0.01, 2]$. Following the clamping, Φ and $\Im(\widetilde{O})$ were smoothed with a 1 pixel wide (full-width at half maximum (FWHM)) Gaussian filter. A self-refining support was additionally included. Beginning from the tenth iteration, a threshold of 0.06 rad was applied to Φ every fifth iteration. Afterwards the support was updated by eroding the reconstruction with a 9 pixel diameter followed by a dilation of 20 pixel diameter. The support was only updated for the first 800 iterations, afterwards it was kept constant for the remaining 10000 iterations. The conventional reconstruction uses equivalent parameters, the $\Im(\widetilde{O})$ range was converted to an amplitude range $A \in [0.14\ 1.01]$.

The results from both reconstructions are shown in Fig. 3. Figure 3(a) shows exemplary a flat-field corrected hologram at a defocus distance of 138.6 mm. The reconstructed amplitudes of the refractive reconstruction are shown in Fig. 3(b) with the corresponding phases shown in Fig. 3(d). The phases of the conventional reconstruction are shown in Fig. 3(c). The ivory sample was prepared by focused-ion-beam milling (FIB), leaving some gallium depositions on the sample surface, visible as the dark rim on the right side of the specimen. The reconstruction is very challenging for conventional PR methods, both for single-step [49] and iterative algorithms: (i) the two components of the sample, ivory and gallium, are very different in their optical properties and (ii) the total phase shift far exceeds π. This is depicted in Fig. 3(e) where line profiles of the conventional and refractive reconstruction are compared. The conventional algorithm does not reach the same phase range as the refractive counterpart. To successfully reconstruct these strongly phase shifting samples, conventional algorithms must be combined with a robust phase unwrapping so that the range clamping and smoothness constraints can be applied. This comes at the price of a (strongly) increased computation time. Once again, the refractive representation aids to circumvent the difficulties in the reconstruction.

5. Coherent Diffraction Imaging

Coherent diffraction imaging (CDI) extents the methodology from X-ray crystallography to non-crystalline, non-periodic samples. The refractive CDI reconstruction is based on the popular difference map (DM) algorithm [53]. In conventional CDI two projectors, P_M and P_S, are used to enforce the measurement and sample constraint, respectively:

$$O_{n+1} = O_n + P_M\left[2P_S\left(O_n\right) - O_n\right] - P_S(O_n). \tag{17}$$

To reconstruct the refractive object $\widetilde{O}$, we introduce the two refractive projectors $\tilde{P}_M$ and $\tilde{P}_S$, similar to NFH. The first projector $\tilde{P}_M$ constrains the reconstruction to fit the measurement. It ensures that the sample has the same Fourier transform as the measured diffraction pattern M:

$$\tilde{P}_M(\widetilde{O}_n) = \widetilde{O}_n - \mathrm{i}\cdot\left[\left(\frac{O_n'}{O_n} - 1\right) - \frac{1}{2}\left(\frac{O_n'}{O_n} - 1\right)^2\right], \tag{18}$$

where the object before O_n and after O_n' the magnitude constraint are given by

$$O_n = \exp(\mathrm{i}\cdot\widetilde{O}_n) \quad \text{and} \quad O_n' = \mathcal{F}^{-1}\left(\sqrt{M}\cdot\frac{\mathcal{F}\left(O_n\right)}{|\mathcal{F}\left(O_n\right)|}\right). \tag{19}$$

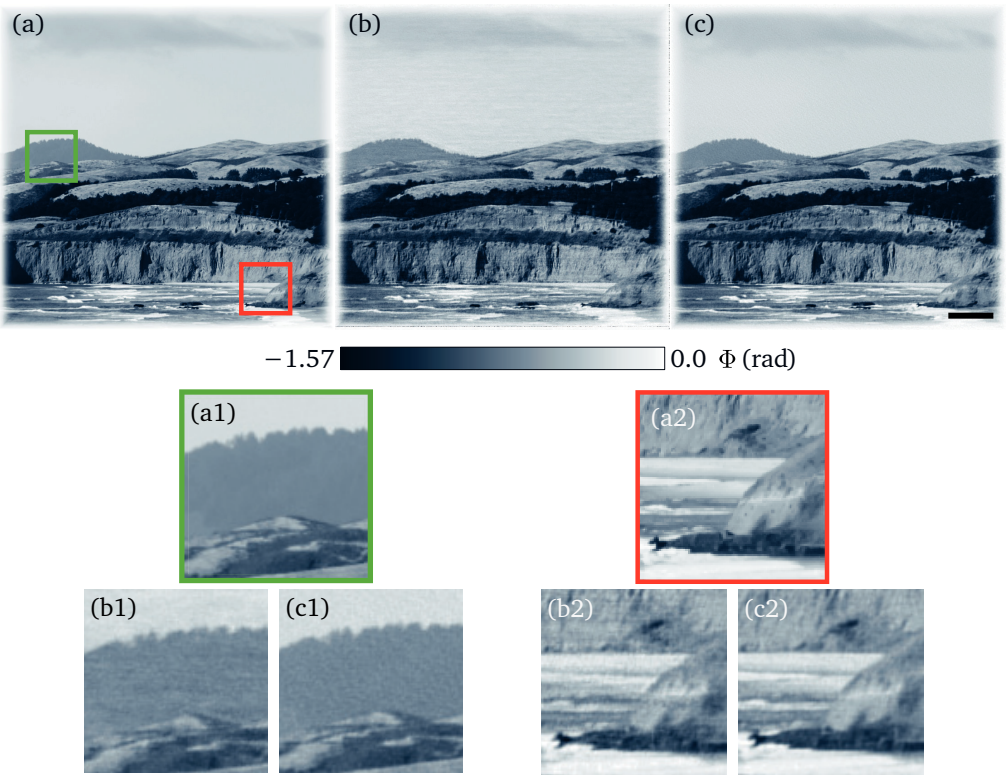

Fig. 4. Results for the CDI simulation. The embedding around the sample is not shown. (a) Original sample. (b) Standard DM reconstruction. (c) Refractive DM reconstruction. The scale bar represents 1 µm. The color bar applies to all panels. Two regions, indicated in (a) by a green and a red box, are shown enlarged in (a1), (b1), (c1) and (a2), (b2), (c2), respectively.

The second projector $\tilde{P}_S$ confines the reconstruction in the sample plane. It ensures that the reconstruction is a pure phase object and confined to the support S:

$$\tilde{P}_S(\tilde{\psi}_n) = \begin{cases} \Re(\tilde{\psi}_{n,\mathbf{r}}) + 0\mathrm{i} & \text{if } \mathbf{r} \in S, \\ 0 + 0\mathrm{i} & \text{if } \mathbf{r} \notin S. \end{cases} \tag{20}$$

A detailed derivation of this method is given in [33].

5.1. CDI Demonstration

To demonstrate the performance of the refractive CDI algorithm, we use a simulated experiment of a weakly scattering phase object. The test sample is a 741×741 pixels coast image, shown in Fig. 4(a), with a maximum phase shift of $\pi/2$ rad. The image is embedded into a uniform, 2048×2048 pixels frame using a Gaussian window function with $\sigma = 20$ pixels. Poisson noise was added to the diffraction pattern equivalent to a photon fluence of 240 photons/nm^2. The parameters of the simulation are collected in Table 3.

We reconstruct the simulated diffraction pattern in two different ways, using the conventional difference map algorithm and the new refractive algorithm. At first glance, the two reconstructions in Fig. 4(b) and (c) appear identical to the original sample. However, the magnified regions marked in green (1) and red (2) highlight the different reconstruction quality. While the refractive

Table 3. Parameters used in the CDI simulation.

Parameters	**Simulation**
Wavelength	1 Å
Detector distance	8192 mm
Detector pixel	40 µm × 40 µm
Detector size	2048 × 2048 pixels
Pixel size (rec.)	10 nm
Object size	7.41 µm × 7.41 µm
Object phase	$[-\pi/2; 0]$
Photons/pixel	23 840

reconstruction shows only weak and diffuse noise, the conventional reconstruction suffers from strong horizontal stripes and is overall much noisier. Consequently, the refractive reconstruction is closer to the ground truth.

6. Summary

We have demonstrated how a refractive framework improves phase retrieval by directly reconstructing the projected refractive index. The refractive framework avoids the amplitude and phase of the transmission function and instead acts on the real and imaginary part of the refractive index. This allows to avoid the common phase wrapping problem, which occurs if the phase shift of the sample is larger than 2π.

Using the refractive framework, we have derived refractive algorithms for ptychography, holography, and coherent diffractive imaging (CDI). We have validated the three algorithms on simulated and experimental data from X-ray microscopy. For CDI, the refractive reconstruction model fits naturally to the pure phase constraint, therefore creating less artifacts in the reconstruction. In this case, the refractive reconstruction surpasses the quality of the conventional reconstruction even if the sample has no phase jumps and is only weakly phase shifting. For conventional ptychography and holography, the strongly phase shifting samples are challenging to reconstruct. With a maximum phase shift of 15 rad, the micrometeorite sample is especially challenging, as it requires two phase jumps. Phase jumps, especially if there are multiple, are often not accurately reconstructed and can give rise to phase vortices. Removing the vortices requires constant monitoring as they might reappear in later iterations [54]. In contrast, the refractive variants are able to reconstruct the samples with high fidelity.

As shown in this article, it is straightforward to implement the refractive framework into existing phase retrieval algorithms. Suitable targets are, e.g., multi-slice [8, 34] and near-field ptychography [54, 55]. With the real and imaginary part of the refractive index at hand, more sophisticated constraints can be applied to the reconstruction, e.g., the sparsity of the recovered image [56, 57]. Multi-wavelength algorithms also benefit from the direct access to the refractive index [58, 59]. The refractive formulation of phase retrieval is an immense aid and will foster further developments for the phase retrieval of complex samples, i.e. multi-material, thick and absorbing objects.

Acknowledgments

We acknowledge DESY (Hamburg, Germany), a member of the Helmholtz Association HGF, for the provision of experimental facilities. Parts of this research were carried out at the PETRA III beamlines P05 and P06. Beamtime was allocated for proposal I-20170864 (P05) and as part of the PETRA III inhouse research of D.B. (P06). We would like to thank Imke Greving for fruitful discussions and collaboration in this and other projects. We thank Fritz Vollrath for providing us with the ivory sample. We thank Jan Garrevoet and Stijn van Malderen for assistance in using P06. This research was supported in part through the Maxwell computational resources operated at DESY.

Disclosure

The authors declare no conflicts of interest.

Data Availability

Data underlying the results presented in this paper are not publicly available at this time but may be obtained from the authors upon reasonable request.

References

1. J. R. Fienup, "Phase retrieval algorithms: a personal tour [invited]," Appl. Opt. **52**, 45 (2012).
2. R. P. Millane, "Phase retrieval in crystallography and optics," J. Opt. Soc. Am. A **7**, 394 (1990).
3. L. Taylor, "The phase retrieval problem," IEEE Transactions on Antennas Propag. **29**, 386–391 (1981).
4. D. R. Luke, J. V. Burke, and R. G. Lyon, "Optical wavefront reconstruction: Theory and numerical methods," SIAM review **44**, 169–224 (2002).
5. Y. Shechtman, Y. C. Eldar, O. Cohen, H. N. Chapman, J. Miao, and M. Segev, "Phase retrieval with application to optical imaging: a contemporary overview," IEEE Signal Process. Mag. **32**, 87–109 (2015).
6. P. A. Midgley and R. E. Dunin-Borkowski, "Electron tomography and holography in materials science," Nat. Mater. **8**, 271–280 (2009).
7. M. Töpperwien, M. Krenkel, K. Müller, and T. Salditt, "Phase-contrast tomography of neuronal tissues: from laboratory-to high resolution synchrotron ct," Proc. SPIE **9967**, 99670T (2016).
8. M. Kahnt, L. Grote, D. Brückner, M. Seyrich, F. Wittwer, D. Koziej, and C. G. Schroer, "Multi-slice ptychography enables high-resolution measurements in extended chemical reactors," Sci. Rep. **11** (2021).
9. T. van de Kamp, P. Vagovič, T. Baumbach, and A. Riedel, "A biological screw in a beetle's leg," Science. **333**, 52–52 (2011).
10. J. Moosmann, A. Ershov, V. Altapova, T. Baumbach, M. S. Prasad, C. LaBonne, X. Xiao, J. Kashef, and R. Hofmann, "X-ray phase-contrast in vivo microtomography probes new aspects of xenopus gastrulation," Nature. **497**, 374–377 (2013).
11. N. V. Petrov, A. A. Gorodetsky, and V. G. Bespalov, "Holography and phase retrieval in terahertz imaging," in *Terahertz Emitters, Receivers, and Applications IV,* M. Razeghi, A. N. Baranov, and J. M. Zavada, eds. (SPIE, 2013).
12. J. Garcia-Sucerquia, W. Xu, S. K. Jericho, P. Klages, M. H. Jericho, and H. J. Kreuzer, "Digital in-line holographic microscopy," Appl. Opt. **45**, 836–850 (2006).
13. H. M. L. Faulkner and J. M. Rodenburg, "Movable aperture lensless transmission microscopy: A novel phase retrieval algorithm," Phys. Rev. Lett. **93**, 023903 (2004).
14. L. Allen, H. Faulkner, M. Oxley, and D. Paganin, "Phase retrieval and aberration correction in the presence of vortices in high-resolution transmission electron microscopy," Ultramicroscopy. **88**, 85–97 (2001).
15. M. Beleggia, M. Schofield, V. Volkov, and Y. Zhu, "On the transport of intensity technique for phase retrieval," Ultramicroscopy. **102**, 37–49 (2004).
16. K. Giewekemeyer, S. P. Krüger, S. Kalbfleisch, M. Bartels, C. Beta, and T. Salditt, "X-ray propagation microscopy of biological cells using waveguides as a quasipoint source," Phys. Rev. A **83**, 023804 (2011).
17. M.-C. Zdora, "State of the art of x-ray speckle-based phase-contrast and dark-field imaging," J. Imaging **4**, 60 (2018).
18. D. Paganin, S. C. Mayo, T. E. Gureyev, P. R. Miller, and S. W. Wilkins, "Simultaneous phase and amplitude extraction from a single defocused image of a homogeneous object," J. Microsc. **206**, 33–40 (2002).
19. D. Gabor, "A new microscopic principle," Nature. **161**, 777–778 (1948).
20. P. Thibault, M. Dierolf, A. Menzel, O. Bunk, C. David, and F. Pfeiffer, "High-Resolution Scanning X-ray Diffraction Microscopy," Science. **321**, 379–382 (2008).
21. M. Guizar-Sicairos, A. Diaz, M. Holler, M. S. Lucas, A. Menzel, R. A. Wepf, and O. Bunk, "Phase tomography from x-ray coherent diffractive imaging projections," Opt. Express **19**, 21345–21357 (2011).

22. M. Stockmar, I. Zanette, M. Dierolf, B. Enders, R. Clare, F. Pfeiffer, P. Cloetens, A. Bonnin, and P. Thibault, "X-ray near-field ptychography for optically thick specimens," Phys. Rev. Appl. **3**, 014005 (2015).
23. A. Gustschin, M. Riedel, K. Taphorn, C. Petrich, W. Gottwald, W. Noichl, M. Busse, S. E. Francis, F. Beckmann, J. U. Hammel, J. Moosmann, P. Thibault, and J. Herzen, "High resolution and sensitivity bi-directional x-ray phase contrast imaging using 2d Talbot array illuminators," arXiv. (2021).
24. S. Chowdhury, M. Chen, R. Eckert, D. Ren, F. Wu, N. Repina, and L. Waller, "High-resolution 3D refractive index microscopy of multiple-scattering samples from intensity images," Optica. **6**, 1211 (2019).
25. M. Kahnt, J. Becher, D. Brückner, Y. Fam, T. Sheppard, T. Weissenberger, F. Wittwer, J.-D. Grunwaldt, W. Schwieger, and C. G. Schroer, "Coupled ptychography and tomography algorithm improves reconstruction of experimental data," Optica. **6**, 1282 (2019).
26. K. Shimomura, M. Hirose, T. Higashino, and Y. Takahashi, "Three-dimensional iterative multislice reconstruction for ptychographic x-ray computed tomography," Opt. Express **26**, 31199 (2018).
27. A. Ruhlandt, M. Krenkel, M. Bartels, and T. Salditt, "Three-dimensional phase retrieval in propagation-based phase-contrast imaging," Phys. Rev. A **89**, 033847 (2014).
28. J. M. Rodenburg, A. C. Hurst, A. G. Cullis, B. R. Dobson, F. Pfeiffer, O. Bunk, C. David, K. Jefimovs, and I. Johnson, "Hard-X-Ray Lensless Imaging of Extended Objects," Phys. Rev. Lett. **98**, 034801 (2007).
29. P. Cloetens, W. Ludwig, J. Baruchel, D. Van Dyck, J. Van Landuyt, J. P. Guigay, and M. Schlenker, "Holotomography: Quantitative phase tomography with micrometer resolution using hard synchrotron radiation x rays," Appl. Phys. Lett. **75**, 2912–2914 (1999).
30. J. Miao, P. Charalambous, J. Kirz, and D. Sayre, "Extending the methodology of X-ray crystallography to allow imaging of micrometre-sized non-crystalline specimens," Nature. **400**, 342–344 (1999).
31. W. Wirtinger, "Zur formalen Theorie der Funktionen von mehr komplexen Veränderlichen." Math. Ann. **97**, 357–375 (1927).
32. A. M. Maiden and J. M. Rodenburg, "An improved ptychographical phase retrieval algorithm for diffractive imaging," Ultramicroscopy. **109**, 1256–1262 (2009).
33. F. Wittwer, "Development and study of refractive phase retrieval and x-ray multibeam ptychography," Ph.D. thesis, Universität Hamburg (2020).
34. A. M. Maiden, M. J. Humphry, and J. M. Rodenburg, "Ptychographic transmission microscopy in three dimensions using a multi-slice approach," J. Opt. Soc. Am. **29**, 1606 (2012).
35. P. Thibault and A. Menzel, "Reconstructing state mixtures from diffraction measurements," Nature. **494**, 68–71 (2013).
36. A. Schropp, D. Brückner, J. Bulda, G. Falkenberg, J. Garrevoet, J. Hagemann, F. Seiboth, K. Spiers, F. Koch, C. David, M. Gambino, M. Veselý, F. Meirer, and C. G. Schroer, "Full-field hard x-ray microscopy based on aberration-corrected be CRLs," in *X-Ray Nanoimaging: Instruments and Methods IV,* B. Lai and A. Somogyi, eds. (SPIE, 2019).
37. X. Huang, K. Lauer, J. N. Clark, W. Xu, E. Nazaretski, R. Harder, I. K. Robinson, and Y. S. Chu, "Fly-scan ptychography," Sci. Reports **5** (2015).
38. J. Deng, Y. S. G. Nashed, S. Chen, N. W. Phillips, T. Peterka, R. Ross, S. Vogt, C. Jacobsen, and D. J. Vine, "Continuous motion scan ptychography: characterization for increased speed in coherent x-ray imaging," Opt. Express **23**, 5438 (2015).
39. P. M. Pelz, M. Guizar-Sicairos, P. Thibault, I. Johnson, M. Holler, and A. Menzel, "On-the-fly scans for X-ray ptychography," Appl. Phys. Lett. **105**, 251101 (2014).
40. J. N. Clark, X. Huang, R. J. Harder, and I. K. Robinson, "Continuous scanning mode for ptychography," Opt. Lett. **39**, 6066–6069 (2014).
41. P. Godard, M. Allain, V. Chamard, and J. Rodenburg, "Noise models for low counting rate coherent diffraction imaging," Opt. Express **20**, 25914 (2012).
42. C. Yang, J. Qian, A. Schirotzek, F. Maia, and S. Marchesini, "Iterative algorithms for ptychographic phase retrieval," arXiv (2011).
43. S. Ruder, "An overview of gradient descent optimization algorithms," arXiv (2017).
44. Y. E. Nesterov, "A method for solving the convex programming problem with convergence rate $O(1/k^2)$," Dokl. Akad. Nauk SSSR **269**, 543–547 (1983).
45. A. Maiden, D. Johnson, and P. Li, "Further improvements to the ptychographical iterative engine," Optica **4**, 736–745 (2017).
46. P. Vagovič, T. Sato, L. Mikeš, G. Mills, R. Graceffa, F. Mattsson, P. Villanueva-Perez, A. Ershov, T. Faragó, J. Uličný, H. Kirkwood, R. Letrun, R. Mokso, M.-C. Zdora, M. P. Olbinado, A. Rack, T. Baumbach, J. Schulz, A. Meents, H. N. Chapman, and A. P. Mancuso, "Megahertz x-ray microscopy at x-ray free-electron laser and synchrotron sources," Optica **6**, 1106 (2019).
47. J. Hagemann, M. Vassholz, H. Hoeppe, M. Osterhoff, J. M. Rosselló, R. Mettin, F. Seiboth, A. Schropp, J. Möller, J. Hallmann, C. Kim, M. Scholz, U. Boesenberg, R. Schaffer, A. Zozulya, W. Lu, R. Shayduk, A. Madsen, C. G. Schroer, and T. Salditt, "Single-pulse phase-contrast imaging at free-electron lasers in the hard x-ray regime," J. Synchrotron Radiat. **28**, 52–63 (2021).
48. J. Hagemann and T. Salditt, "The fluence–resolution relationship in holographic and coherent diffractive imaging," J. Appl. Crystallogr. **50**, 531–538 (2017).
49. P. Cloetens, R. Barrett, J. Baruchel, J.-P. Guigay, and M. Schlenker, "Phase objects in synchrotron radiation hard

x-ray imaging," J. Phys. D: Appl. Phys. **29**, 133–146 (1996).
50. L. M. Lohse, A.-L. Robisch, M. Töpperwien, S. Maretzke, M. Krenkel, J. Hagemann, and T. Salditt, "A phase-retrieval toolbox for x-ray holography and tomography," J. Synchrotron Radiat. **27** (2020).
51. L. Lohse, A.-L. Robisch, M. Töpperwien, S. Maretzke, M. Krenkel, J. Hagemann, and T. Salditt, "Holotomotoolbox online repository," https://gitlab.gwdg.de/irp/holotomotoolbox (2020).
52. S. Flenner, A. Kubec, C. David, M. Storm, C. F. Schaber, F. Vollrath, M. Müller, I. Greving, and J. Hagemann, "Hard x-ray nano-holotomography with a Fresnel zone plate," Opt. Express **28**, 37514 (2020).
53. V. Elser, "Phase retrieval by iterated projections," J. Opt. Soc. Am. A **20**, 40–55 (2003).
54. M. Stockmar, P. Cloetens, I. Zanette, B. Enders, M. Dierolf, F. Pfeiffer, and P. Thibault, "Near-field ptychography: phase retrieval for inline holography using a structured illumination," Sci. Rep. **3**, 1927 (2013).
55. A.-L. Robisch, K. Kröger, A. Rack, and T. Salditt, "Near-field ptychography using lateral and longitudinal shifts," New J. Phys. **17**, 073033 (2015).
56. A. Pein, S. Loock, G. Plonka, and T. Salditt, "Using sparsity information for iterative phase retrieval in x-ray propagation imaging," Opt. Express **24**, 8332–8343 (2016).
57. N. H. Thao, D. R. Luke, O. Soloviev, and M. Verhaegen, "Phase retrieval with sparse phase constraint," SIAM J. on Math. Data Sci. **2**, 246–263 (2020).
58. M. Hirose, K. Shimomura, N. Burdet, and Y. Takahashi, "Use of Kramers–Kronig relation in phase retrieval calculation in X-ray spectro-ptychography," Opt. Express **25**, 8593–8603 (2017).
59. A.-L. Robisch, M. Eckermann, M. Töpperwien, F. van der Meer, C. Stadelmann-Nessler, and T. Salditt, "Nanoscale x-ray holotomography of human brain tissue with phase retrieval based on multienergy recordings," J. Med. Imaging **7**, 1 (2020).